

JGR Atmospheres

RESEARCH ARTICLE

10.1029/2021JD035182

Key Points:

- In-situ measurements of supercooled liquid water in a cloud at temperatures as low as 240 K are presented
- Polar measurements support laboratory results demonstrating that the liquid-water complex refractive index is temperature dependent
- Radiative transfer through supercooled liquid cloud is sensitive to the temperature dependence of the liquid-water complex refractive index

Supporting Information:

Supporting Information may be found in the online version of this article.

Correspondence to:

P. M. Rowe,
penny@nwra.com

Citation:

Rowe, P. M., Walden, V. P., Brandt, R. E., Town, M. S., Hudson, S. R., & Neshyba, S. (2022). Evaluation of temperature-dependent complex refractive indices of supercooled liquid water using downwelling radiance and in-situ cloud measurements at South Pole. *Journal of Geophysical Research: Atmospheres*, 127, e2021JD035182. <https://doi.org/10.1029/2021JD035182>

Received 30 APR 2021
Accepted 8 DEC 2021

Evaluation of Temperature-Dependent Complex Refractive Indices of Supercooled Liquid Water Using Downwelling Radiance and In-Situ Cloud Measurements at South Pole

Penny M. Rowe¹ , Von P. Walden² , Richard E. Brandt^{3,4}, Michael S. Town⁵, Stephen R. Hudson⁶ , and Steven Neshyba⁷ 

¹NorthWest Research Associates, Redmond, WA, USA, ²Washington State University, Pullman, WA, USA, ³Atmospheric Sciences Research Center, University at Albany, Albany, NY, USA, ⁴University of Washington, Seattle, WA, USA, ⁵Geophysical Institute and Bjerknes Centre for Climate Research, University of Bergen, Bergen, Norway, ⁶Norwegian Polar Institute, Tromsø, Norway, ⁷University of Puget Sound, Tacoma, WA, USA

Abstract Clouds have a large effect on the radiation budget and represent a major source of uncertainty in climate models. Supercooled liquid clouds can exist at temperatures as low as 235 K, and the radiative effect of these clouds depends on the complex refractive index (CRI) of liquid water. Laboratory measurements have demonstrated that the liquid-water CRI is temperature-dependent, but corroboration with field measurements is difficult. Here we present measurements of the downwelling infrared radiance and in-situ measurements of supercooled liquid water in a cloud at temperatures as low as 240 K, made at South Pole Station in 2001. These results demonstrate that including the temperature dependence of the liquid-water CRI is essential for accurate calculations of radiative transfer through supercooled liquid clouds. Furthermore, we show that when cloud properties are retrieved from infrared radiances (using the spectral range 500–1,200 cm⁻¹) spurious ice may be retrieved if the 300 K CRI is used for cold liquid clouds (~240 K). These results have implications for radiative transfer in climate models as well as for retrievals of cloud properties from infrared radiance spectra.

Plain Language Summary Clouds cause both a cooling effect, through reflecting sunlight away from the Earth, and a warming effect, through trapping infrared radiation (i.e., the greenhouse effect). “Supercooled” liquid droplets can exist in clouds at temperatures well below 0°C. Here we present images of liquid water in clouds over the South Pole, captured by flying a video camera on a balloon, at temperatures as low as -33°C. Prior laboratory measurements have indicated that the trapping efficiency of such cold clouds is different from that of warmer clouds due to changes in the index of refraction of liquid water with temperature. We provide further evidence for this temperature dependence by comparing measurements and simulations of the infrared radiation emitted by the cloud during the balloon flight.

1. Introduction

Clouds represent a major source of uncertainty in climate models (Boucher et al., 2013). Clouds have a strong impact on the radiation budget, which is sensitive to thermodynamic phase. In particular, water droplets can exist as supercooled liquid clouds at temperatures as low as 235 K (Koop et al., 2000), and are common both in single-phase and in mixed-phase clouds in polar regions, where they play a significant role in energy balance, with important implications for climate (Cesana et al., 2012; Cox et al., 2015; Lawson & Gettelman, 2014). Supercooled liquid also occurs in clouds globally (e.g., Hogan et al., 2003; Hu et al., 2010; Rosenfeld & Woodrley, 2000; Zhang et al., 2010).

The impact of supercooled liquid clouds on the radiation budget depends on the complex refractive index (CRI) of liquid water. Laboratory measurements have demonstrated that the CRI is temperature-dependent in the infrared region, becoming more similar to ice as temperature decreases from 300 K down to 240 K (Wagner et al., 2005; Zasetsky et al., 2005). In particular, a major peak in the imaginary part of the CRI shifts from about 550 cm⁻¹ for liquid water at 300 K to about 700 cm⁻¹ at 240 K (the ice peak is at ~800 cm⁻¹), as shown in Figure 1. Rowe et al. (2013, 2020) showed that failing to account for changes in the CRI with temperature leads to spectrally dependent biases in liquid-cloud fluxes and underestimation of the overall greenhouse effect of supercooled liquid clouds, highlighting the importance of including this temperature dependence in climate models. However, corroboration of laboratory measurements with measurements of cloud infrared radiation is

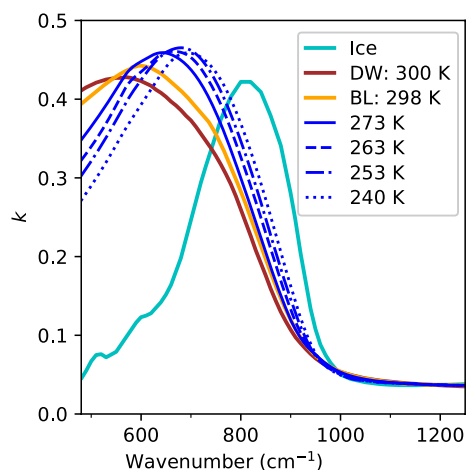


Figure 1. Imaginary part (k) of the complex refractive index of water ice at 240 K (ice; Warren & Brandt, 2008) and for liquid water at temperatures of 300 K (DW; Downing & Williams, 1975), 298 K (BL; Bertie & Lan, 1996), and from 273 to 240 K (Rowe et al., 2020).

difficult due to the necessity of carefully characterizing the cloud properties and atmospheric state.

In this paper, we use data from the South Pole Atmospheric Radiation and Cloud Lidar Experiment (SPARCLE) to study the properties of supercooled water clouds at temperatures near 240 K. Because surface temperatures at the South Pole are so low, South Pole can serve as a natural laboratory for studying low-temperature clouds. SPARCLE took place during austral summer 1999/2000, followed by a full year in 2001, at South Pole Station (Walden et al., 2001). A major goal of SPARCLE was to study longwave radiation and how it relates to climate processes.

On 2 February 2001, in-situ measurements of supercooled liquid droplets were made (similar to those of Lawson et al., 2011), by imaging liquid droplets during a flight through an ice-free cloud at ~ 240 K. The size distribution of the liquid droplets was then determined. Here, we use these measurements, together with concurrent downwelling radiance measurements and measurements characterizing the atmosphere (e.g., in-situ temperature and humidity; surface CO_2 ; micropulse lidar) to show that accurate simulation of the downwelling radiance of this supercooled liquid cloud requires the use of supercooled liquid-water CRI.

2. Measurements

2.1. In-Situ Cloud Particle Measurements

Cloud particles were measured in-situ using a hydrometeor videonode (HYVIS; Murakami & Matsuo, 1990; Orikasa & Murakami, 1997), shown in Figure 2 (reproduced from Walden et al., 2005). The HYVIS was described by Walden et al. (2001, 2005) and is thus described briefly here. During flight, cloud particles were drawn into the top half of the HYVIS (black tube on top of metal cover in Figure 2). The flow rate, estimated to be 29.2 ± 3.2 L/min at STP, as determined in the laboratory by A. Hills and A. Heymsfield (personal communication, 2005) was adjusted to the temperatures and pressures experienced during HYVIS flights at South Pole.

The cloud particles adhered to silicone-coated tape inside the HYVIS and were illuminated by a lamp. The tape was alternately video-recorded by a near-angle camera at high-resolution ($7\times$) and by a wide-angle camera at low resolution ($0.33\times$); the video cameras were housed in the bottom half of the HYVIS (white Styrofoam in Figure 2). Finally, the images were transmitted to a receiver and stored digitally.

The HYVIS was flown together with a radiosonde (Vaisala RS-80) for making concurrent in situ measurements of temperature, humidity, and pressure (see Walden et al., 2005 for additional details).

For the in situ measurements described in this work, the HYVIS was flown from a tethered balloon (AIR, Inc., Boulder, CO), shown in Figure 3, which typically reached a height of 300–400 m above ground level.

During an 18-min section of a flight through a low-lying cloud on 2 February 2001, liquid droplets are evident in the images from the HYVIS, while ice crystals are absent. This flight segment includes 66 HYVIS images. Two of the images are shown in Figure 4 (reproduced from Walden et al., 2005). The two images were taken at the same magnification ($7\times$), approximately 6 min apart (at 02:59:41 and 03:05:54 UT; note that the times on the images are relative to 02:30 UT). Streaks in the silicone oil are evident as white lines, while dark circles correspond to droplets. Comparing the upper and lower panels, it is evident that droplet sizes are larger and droplet concentrations are smaller in the lower panel (Figure 4b). These changes correspond to moving

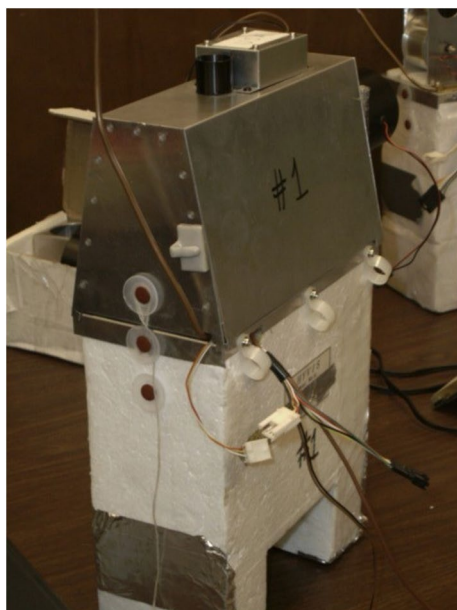


Figure 2. The hydrometeor videonode (HYVIS) instrument, used to capture in-situ images of cloud particles.

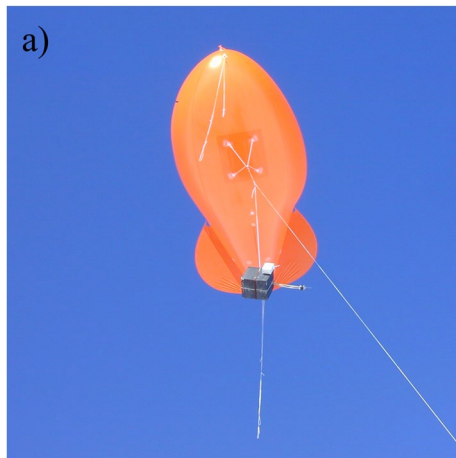


Figure 3. The tethered balloon from which in situ videosonde and radiosonde measurements were made at South Pole in 2000/2001. [The image of the tethered balloon was taken by Jeff Inglis for the *Antarctic Sun*.]

up through the cloud ~ 100 m; between the times of the images, the balloon ascended from 270 to 380 m above the surface (3,085–3,215 m above sea level).

The pressure, temperature, and relative humidity during the flight are shown in Figure 5 (reproduced from Walden et al., 2005). The balloon started at the surface at the beginning of the time period (~ 695 hPa), ascended to a height of ~ 450 m (~ 650 hPa), and then descended to the surface again. The dashed lines indicate the times corresponding to the images shown in Figure 4. After the first image was taken, the temperature had begun increasing with height, indicating the presence of an aloft temperature inversion, and relative humidities with respect to water were 95%–100%. Temperatures were ~ 241 K, just above the extreme-low limit where supercooled water is possible.

True relative humidity values were likely to be slightly higher than those measured with the radiosonde, given that Vaisala RS80 relative humidity measurements are known to have a daytime dry bias. This bias was estimated to be 20%–24% at Dome C, Antarctica at solar zenith angles of 62° (Rowe et al., 2008). The bias in this work is probably smaller because solar zenith angles were 73.1° . Thus actual relative humidity values may be at or above supersaturation with respect to liquid water.

Based on the droplets observed, as well as micropulse lidar data (Mahesh et al., 2005; Spinhirne, 1993; Section S1 in Supporting Information S1) during this time period that indicated the presence of a single-layer cloud extending from about 260 to 470 m above the surface (2835 m), a liquid-only cloud is assumed to exist between 3,095 and 3,305 m above sea level. The micropulse lidar data shows that the cloud vertical extent was fairly stable during 5 hr encompassing the time period, with a cloud base of 250–280 and cloud top of 400–550 m (see Figure S2a in Supporting Information S1 from 0100 until 0600 UTC; an expanded view during the flight time is given in Figure S2b in Supporting Information S1). During the descent back down through the cloud, both liquid and ice hydrometeors were observed; this coincides with a drop in relative humidity during the descent, from about 0320 UTC on (Figure 5). To minimize the likelihood of ice during the radiance measurement, we use the first measurement occurring after the balloon entered the cloud. Thus the maximum time difference between the HYVIS ascent up through the cloud and the time of the radiance measurement is 18 min.

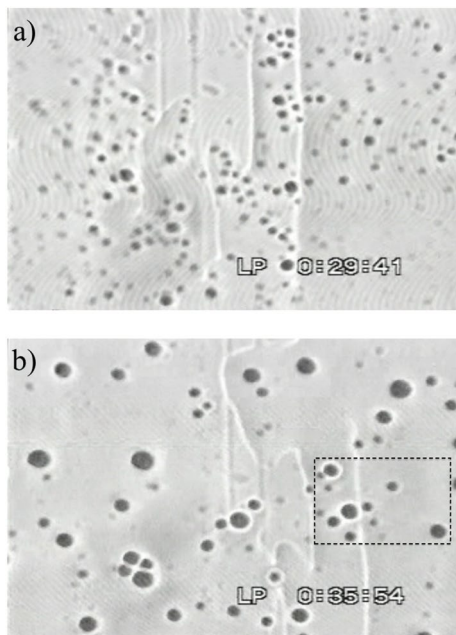


Figure 4. In-situ images of cloud droplets taken by a hydrometer videosonde over South Pole on 2 February 2001. The elapsed time from 0230 UT is shown in each panel. Supercooled water droplets are evident as black circles. The true image dimensions are approximately 1.6 by 1.1 mm (width by height). The dashed box is expanded in Figure 6.

2.2. Surface-Based Infrared Radiance Measurements

Downwelling infrared radiances were measured from the South Pole surface using the Polar Atmospheric Emitted Radiance Interferometer (PAERI) in December 2000 and during most of 2001. The PAERI measures downwelling radiance from ~ 500 to $3,000$ cm^{-1} at a resolution of 0.5 cm^{-1} and has been described and characterized in a number of papers (Rowe et al., 2006, 2009; Rowe, Neshyba, Cox, & Walden, 2011; Rowe, Neshyba & Walden, 2011; see also references therein). Here we use PAERI measurements made on 2 February 2001.

Random instrument error (noise) was calculated as in Rowe, Neshyba and Walden (2011, see Equation 6), and was found to be <0.05 RU (1 RU $\equiv 1$ $\text{mW}/[\text{m}^2 \text{sr cm}^{-1}]$); after averaging within microwindows (Rowe et al., 2019), random errors were reduced to <0.02 RU. Total systematic instrument errors (one standard deviation) were estimated by Rowe et al. (2008) to be <0.1 RU over the spectral range used in this study, from 492 to $1,200$ cm^{-1} . However, laboratory measurements following the field season revealed an additional source of systematic error, which was characterized by comparing simulated radiances to 41 radiance measurements occurring during clear-sky periods

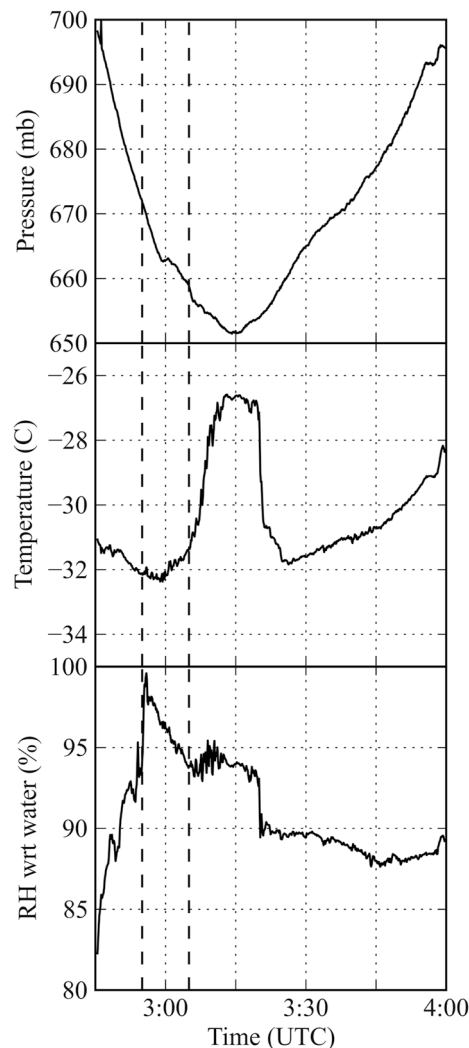


Figure 5. Pressure, temperature, and relative humidity with respect to water measured in situ in the atmosphere above South Pole Station on 2 February 2001. Images of cloud droplets taken at the times indicated by the vertical dashed lines are discussed in the text.

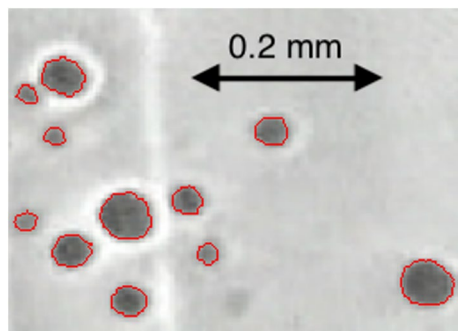


Figure 6. Image of water droplets on silicone-coated tape, captured in situ in a cloud above South Pole Station on 2 February 2001. Droplet boundaries are shown in red and are identified as described in the text.

within 10–24 UT on 2001/2/2. This analysis, described in the Supplemental, indicates the presence of a calibration bias that increases in magnitude as the scene-view brightness temperature decreases below the temperature of the ambient blackbody. Thus, while measured radiances are found to be biased low by as much as 1 RU in microwindows when skies are clear, the bias is considerably smaller when skies are partially opaque (e.g., at wavenumbers where CO₂ or water vapor are strong emitters, or in the presence of clouds). Based on this analysis, estimates of systematic errors were increased to 0.14–0.20 RU.

3. Methods

3.1. Cloud Particle Size Distributions

The image analysis described in this section follows that given by Walden et al. (2005). Frames containing liquid droplets were identified visually. Video sampled at 10 frames per second was converted to Tagged Image File Format (TIFF) files containing still images. Images were then selected that corresponded to the high-magnification video camera, spaced ~17–18 s apart. The spacing was chosen such that selected times occurred immediately before the video tape advanced, in order to capture the greatest number of hydrometeors.

Next, water droplets were discriminated from the silicone-streaked image background. Because the background intensity varied, due to variations in illumination intensity and silicone thickness, it was determined for each image. The Matlab (The Mathworks, Natick, MA) image processing toolbox (IPT) was used to set a threshold value for the background intensity, following the method of Otsu (1979). A corresponding black and white image was then created in which pixels with values below the threshold were set to white and all other pixels were set to black. Following this, the IPT was used to identify black objects in the image. For each object, the total pixel area was determined, along with the major and minor axes, centroid and eccentricity. Finally, the eccentricity of the objects (ϵ) was used to remove anomalous results, such as dark regions of the background, single pixels, or droplets with overlapping borders.

An example of the resulting identification is shown in Figure 6 (corresponding to the dashed box shown in Figure 4b previously). Boundaries of identified water droplets are indicated in red.

The eccentricities of ~2700 objects identified in images collected over South Pole Station on 2 February 2001 are shown in Figure 7. Objects with $\epsilon = 0$, corresponding to perfect circles, were typically just a few pixels or less and were assumed to be anomalies (gray shading at $\epsilon = 0$ in Figure 7). These objects had major axes $< \sim 5$ micrometers (corresponding to airborne radii $< \sim 1.2$ micrometers (see Equation 1 below). At the opposite extreme, objects with $\epsilon > 0.8$ were visually identified as typically corresponding to thick layers of silicone oil, creating dark, jagged lines (gray shading at $\epsilon > 0.8$ in figure; note that $\epsilon = 1$ corresponds to a line). The remaining objects were assumed to correspond to water droplets, with a median eccentricity of ~ 0.45 .

To determine the radii of the water droplets, first a scale factor was determined for converting from pixels to μm . A scale factor of 2.3 micrometers per pixel was determined from images of a ruler using the high-magnification camera (Walden et al., 2005). By measuring the HYVIS image of the ruler scale multiple times, then determining the average and standard deviation of

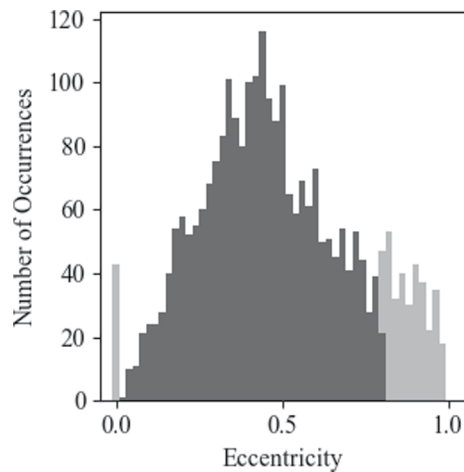


Figure 7. Histogram of eccentricities of objects identified in images from video-recordings made in situ in the atmosphere above South Pole Station on 2 February 2001. Objects are assumed to correspond to water droplets except for anomalous values indicated by gray shading.

the distances, the uncertainty in the scale factor was estimated to be <1%. Using the scale factor to convert to micrometers, the droplet diameter was determined from the mean of the major and minor axes. This was then divided by two to get the radius.

Next, to convert the impacted-droplet radius to the droplet radius in the cloud, a relationship determined in laboratory experiments was used (see Walden et al., 2005). The radius of impacted droplets r_i was found to be related to that of airborne water droplets, r_a , by

$$r_a = 0.486 r_i. \quad (1)$$

The airborne radii from the flight upward through the cloud are then binned in 1-micron bins to give the number density $n(r_a)$.

Following Hansen and Travis (1974), the “effective radius” for radiative properties is calculated from r_a and the associated droplet size distribution, $n(r_a)$, as

$$r_e = \left(\int_0^\infty r_a^3 n(r_a) dr_a \right) / \left(\int_0^\infty r_a^2 n(r_a) dr_a \right) \quad (2)$$

3.2. Downwelling Infrared Radiance Simulations

Downwelling radiances were simulated for the following combinations of cloud phase and single-scattering parameters: (a) ice-only clouds using the ice CRI of Warren and Brandt (2008), assuming equivalent spheres (Grenfell & Warren, 1999); (b) liquid-only cloud using the liquid CRI of Downing and Williams (1975), based on measurements made near 300 K, (c) liquid-only cloud using a new hybrid liquid CRI based on measurements made at temperatures near 240 K (Rowe et al., 2020); and (d) mixed-phase cloud using a combination of the 300 and 240 K CRI. Single-scattering parameters were determined from the complex indices of refraction using Mie theory; more details are given in Cox et al. (2016; Section 2) and Rowe et al. (2020).

Downwelling radiances were simulated using a code developed for this purpose named run_disort (https://bitbucket.org/clarragroup/rundisort_py; Rowe et al., 2019), which takes as inputs the atmospheric temperature, gaseous optical depths, cloud properties, liquid- and ice-water single scattering parameters, and other necessary inputs, and runs the Discrete Ordinates Radiative Transfer (DISORT) code (Stamnes et al., 1988), with a minimum of 16 streams.

Gaseous optical depths were created using LBLRTM (v. 12.8; Clough et al., 2005). LBLRTM requires atmospheric profiles that characterize the atmospheric state in terms of temperature, pressure, and trace gas concentrations. To create these profiles, measurements of temperature, pressure, and humidity made during the tethered balloon flight were used. Values above the maximum height achieved by the tethered balloon were determined from a routine radiosonde launched by the South Pole meteorological office on 2 February 2001 at 0828 UTC. Water vapor above 9 km was set to 5 ppm. The CO₂ surface concentration was based on surface flask measurements (Conway et al., 1994) made by the Climate Monitoring and Diagnostics Laboratory (CMDL) of the National Oceanic and Atmospheric Administration (NOAA), and the shape of the vertical profile was determined from CarbonTracker (Peters et al., 2007). Ozone concentrations from ozonesondes launched on 28 January 2001 at 2128 UTC and 4 February 2001 at 2056 UTC were interpolated to the time of the HYVIS measurements. These gaseous optical depths created with LBLRTM were modified to account for the instrument resolution as described by Rowe et al. (2019).

The cloud vertical extent was assumed based on in situ measurements to be 260–470 m above the surface (3.085–3.3 km), as discussed previously. Additional cloud properties needed for simulating the downwelling radiance include cloud optical depth, ice fraction, effective radius of liquid, and effective radius of ice. These cloud properties were retrieved from AERI radiances measured within a few hours of the tethered balloon sounding, using the CCloud and Atmospheric Radiation Retrieval Algorithm (CLARRA; Rowe et al., 2019). CLARRA uses an optimal Bayesian method for iterative retrieval, following the Levenberg-Marquardt method (Rodgers, 2000;

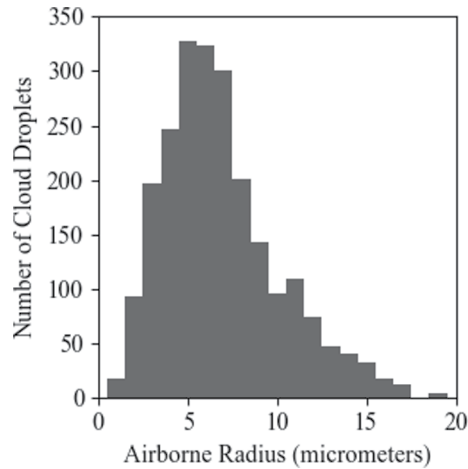


Figure 8. Number of cloud droplets identified in images taken in situ in the atmosphere above South Pole Station on 2 February 2001.

Rowe et al., 2019). Cloud properties were retrieved separately for each of the combinations of cloud phase and single-scattering parameters described above. For single-phase runs the ice fraction was fixed at 0 (combination a) or 1 (combinations b and c) and only the effective radius of the phase present was retrieved, while for mixed-phase runs all four cloud properties were retrieved. The inverse retrieval optimizes the retrieved cloud properties for each set, given the estimated errors in the measurement and the simulation.

Retrieving cloud properties for each combination of single-scattering parameter and cloud phase means that the cloud properties used in creating the simulations vary. Moreover, they are optimized such that the difference between the resulting simulated radiance and the measurement for each combination is as small as possible (given the a priori values). Thus we err on the side of *underestimating*, rather than overestimating, differences between simulation and measurement due to using incorrect cloud properties. This also means that the closeness of the retrieved effective radius of liquid water to the measured effective radius can serve as an indicator of accuracy.

Uncertainties in simulated radiances were estimated based on uncertainty estimates of 0.5 K for temperature and 5% for gaseous optical depth, which approximates uncertainties in each trace gas of 5%.

4. Results

Figure 8 shows the size distribution of all identified supercooled water droplets from the in-situ measurement on 2 February 2001. The mode radius is about 5.5 μm and the range is $\sim 2\text{--}20$ μm . The effective radius of the distribution, calculated according to Equation 2, is 10 μm . The collection efficiency of the HYVIS may result in small errors in the number of droplets with small radii. Failure to identify droplets, or misidentifications, can also result in inaccuracies in the effective radius determined.

Comparisons of simulated radiance spectra to the measured spectrum (plotted as brightness temperature) from 2 February 2001 at 0307 UTC are shown in Figure 9. The legend indicates the phase and, for simulations including liquid (liq and mix), the temperature corresponding to the liquid-water single scattering parameters. Error bars indicate the combined uncertainty in measured and simulated radiances (1 standard deviation); they are shown relative to the measured radiance for clarity. Orange triangles that are obscured are behind the black circles; see also Figure S8 in Supporting Information S1, where they are all visible. Recall that each simulated spectrum shown uses the optimal cloud optical depth and effective radius, retrieved from the measurement using CLARRA (for the mixed-phase case, ice fraction was also retrieved and effective radii for both ice and liquid were retrieved). These are given in Table 1. Thus, each simulated spectrum indicates the optimal fit to the measurement for the given phase (or phases) and single-scattering parameters.

Not surprisingly, given that no ice was observed in the in-situ measurements, the worst agreement is achieved when an ice-only cloud is used (cyan squares). Agreement is considerably better when liquid-only droplets are retrieved using the 300 K CRI (green stars), but agreement is worse than expected uncertainties for many points (Table 1 gives the rms difference in RU). Furthermore, the brightness temperature is too low from 750 to 900 cm^{-1} and too high from 1,050 to 1,200 cm^{-1} , and the optimal effective radius (7.8 μm) is smaller than that determined from the in-situ measurements (10 μm). Agreement further improves if the retrieval uses the 300 K CRI for liquid water and allows for mixed-phase cloud (mix, 300 K; orange triangles), although many points still fall outside the uncertainty limits.

Best agreement is achieved when the 240 K CRI is used to retrieve liquid-only cloud properties (black circles), with most points agreeing to within the error at the 1 standard deviation level. The optimal effective radius retrieved (8.3 μm) is also closer to the value for the in-situ measurements (10 μm).

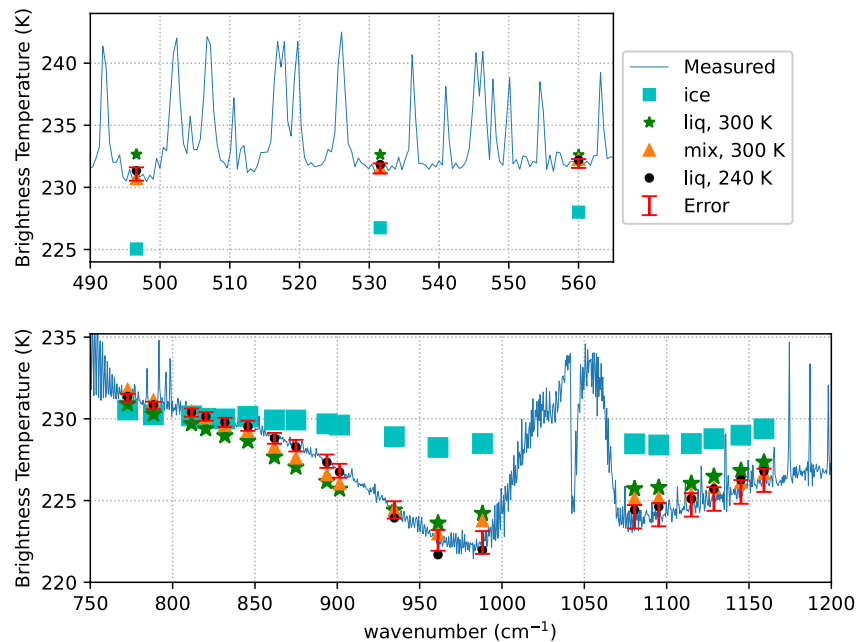


Figure 9. Brightness temperature corresponding to downwelling radiance spectra measured at South Pole Station on 2 February 2001 at 0307 UT (Measured) compared to simulations made using complex refractive indices for: ice, liquid-water based on measurements made at 300 K (liq, 300 K), ice and liquid-water based on measurements made at 300 K (mix, 300 K), and for liquid-water based on measurements made at 240 K (liq, 240 K). Red error bars show combined measurement and simulation error.

5. Discussion

5.1. Cloud Properties

The in-situ cloud properties observed in this work are consistent with those observed by Lawson et al. (2011), who also observed supercooled liquid water in clouds over South Pole (in summer 2009). They found liquid water at cloud top at similar temperatures (241 K). However, their observed effective radii were smaller, with a range of $\sim 3.5\text{--}9.2\ \mu\text{m}$, compared to the in-situ result for this work ($10\ \mu\text{m}$). As stated previously, it is possible that the effective radius retrieved here was slightly overestimated due to a lower collection efficiency of the HYVIS for small droplets. Slightly smaller effective radii ($4.9\text{--}8.1\ \mu\text{m}$) were retrieved from the downwelling infrared radiance spectra within a few hours of the tethered balloon flight, consistent with Lawson et al. (2011).

Table 1

Cloud Properties Retrieved From PAERI Spectra Measured at South Pole Station, Antarctica, on 2001/02/02, for Sets of Liquid Complex Refractive Indices Based on Measurements Made at the Temperature Indicated (T Liq CRI)

Phase	T Liq CRI(K)	Optical depth	f_{ice}	$r_{\text{liq}}\ (\mu\text{m})$	$r_{\text{ice}}\ (\mu\text{m})$	LWP(g/m ²)	RMS diff(RU)
Liquid	300	2.5	0	7.8	–	12.7	0.8
Ice	–	2.6	1	–	18	0.0	2.6
Mix	300	2.6	0.3	6.3	8.0	7.5	0.23
Liquid	240	2.3	0	8.3	–	12.5	0.20
Mix	240	2.4	0.06	7.9	28	11.6	0.18

Note. For each case, the cloud phase was constrained to be either liquid, ice, or mixed (first column); for mixed phase clouds the ice fraction (f_{ice}) was also retrieved. The retrieved cloud properties are: cloud optical depth referenced to the visible is given as od, and the effective radii of liquid and ice are given as r_{liq} and r_{ice} . The root-mean-square difference between measured and retrieved radiances in units of mW/(m² sr cm⁻¹), or RU, is given in the final column (RMS diff).

5.2. Complex Refractive Indices

The infrared spectrum simulated for an ice-only cloud was found to be too low from 490 to 800 cm^{-1} and too high from 850 to 1,175 cm^{-1} (cyan squares in Figure 9; recall that the simulation used the same atmospheric state and cloud height as measured in situ, but ice-only phase was fixed while optical depth and effective radius were optimized for agreement with the measured spectrum). However, the opposite spectral trend was found if the phase was instead fixed to liquid-only, and the 300 K liquid-water CRI was used. This suggests that adding ice to the model can to a large degree compensate for using the 300 K liquid-water CRI for a supercooled cloud. Further supporting this, the figure shows that differences between measured and simulated radiances are significantly reduced if mixed phase clouds are retrieved, to a root-mean-square difference of 0.2 RU, which is similar to that for liquid-only clouds with the correct CRI (Table 1). This finding is in keeping with expectations of Zsazsky et al. (2004), who indicate that a reasonable approximation to supercooled liquid CRI is a combination of warm liquid-water CRI and ice-water CRI.

The compensation described above has important consequences, because it indicates that using the incorrect CRI for supercooled liquid water can result in spurious ice retrieval. Indeed, when the 300 K CRI is used and mixed-phase clouds are permitted, a significant amount of ice is retrieved for this case (30% of the optical depth is estimated to be due to ice; see Table 1). Furthermore, the retrieved ice effective radius (8 μm) is similar to that expected for liquid. This negatively biases the retrieved liquid effective radius, which is reduced from 8.3 μm (for liquid-only cloud using the 240 K CRI) to 6.3 μm , and positively biases the optical depth, which is increased from 2.3 to 2.6. Thus, if the incorrect CRI is used, the results may appear reasonable, but biases will be incurred.

In contrast to the above, when the 240 K single scattering parameters are used, cloud phase is retrieved with high accuracy. The retrieved ice fraction is small (6%). This indicates that for supercooled liquid clouds, given similar uncertainty levels, retrievals of spurious ice can be avoided by using single-scattering parameters corresponding to the correct cloud temperature.

6. Conclusions

Here we present in situ measurements of supercooled liquid water at temperatures as low as 240 K from a summertime cloud over South Pole station in 2001, together with corresponding downwelling infrared radiance spectra and cloud-property retrievals. Analysis of in-situ images from a hydrometeor videosonde flown in the cloud suggests the droplets had a mode radius of 5.5 μm , a range of 2–20 μm , and an effective radius of 10 μm .

Cloud properties were retrieved from the radiance measurements using the CLOUD and Atmospheric Radiation Retrieval Algorithm (CLARRA). Retrievals used single scattering properties based on CRI measurements made at the cloud temperature (near 240 K), as well as the CRI that has typically been used in retrievals, which are based on measurements made at ~ 300 K. The results demonstrate that using the CRI for the cloud temperature results in much better agreement between measured and simulated spectra. Furthermore, the results demonstrate that using the CRI based on the incorrect temperature results in spurious ice retrieval in supercooled-liquid clouds, highlighting the importance of including the temperature dependence of the CRI for accurate calculations of radiative transfer through supercooled liquid clouds. Thus, we recommend using temperature-dependent CRI in radiative transfer calculations and infrared retrievals of liquid-water cloud, which have been compiled by Rowe et al. (2020; see Data for availability). These results have implications for retrievals of cloud properties from infrared radiance spectra, and likely also have important implications for radiative transfer in climate models (e.g., Rowe et al., 2013).

Conflict of Interest

The authors declare no conflicts of interest relevant to this study.

Data Availability Statement

Computer code used in the analysis is available at <https://bitbucket.org/clarragroup/>. Other computer code and data are available on request. Temperature-dependent complex refractive indices for 240 K are available at <https://refractiveindex.info/?shelf=main&book=H2O&page=Rowe-240K>; for other temperatures replace 240 K with

253, 263, or 273 K. Corresponding single-scattering parameters are available at people.nwra.com/rowe/single_scatter.shtml. Measured data have been submitted to the PANGAEA archive and will be available shortly.

Acknowledgments

The authors are grateful to Andy Heymsfield (National Center for Atmospheric Research; NCAR) for lending two hydrometeor vide sondes as well as receiving equipment for this project. Mark Ellison from the University of Idaho processed the HYVIS images to determine the sizes of hydrometeors. The authors thank Hal Cole (NCAR) for loaning us a 403-MHz receiver for acquiring Vaisala radiosonde data and Alan Hills and Andy Heymsfield of NCAR for characterizing the size relationship between airborne and impacted droplets in laboratory measurements. The authors thank Stephen Warren for assistance and advice during the fieldwork and for manuscript editing. The authors are grateful to Richard Jones for valuable help with the HYVIS flights, to NOAA CMDL for CO₂ measurements and to CarbonTracker for CO₂ vertical structure and upper tropospheric temperatures (version CT2017, NOAA ESRL; <http://carbon-tracker.noaa.gov>; Peters et al., 2007). Support for this research came from the NSF Office of Polar Programs through grants OPP-02-30114, OPP-97-26676, OPP-02-30466, and award 2127632, as well as the Teacher's Experiencing Antarctica (TEA) program. Simulations of downwelling radiance for different CRI were created using support from the NSF Office of Polar Programs grant 1543236.

References

- Bertie, J. E., & Lan, Z. (1996). Infrared intensities of liquids XX: The intensity of the OH stretching band of liquid water revisited, and the best current values of the optical constants of H₂O (l) at 25°C between 15,000 and 1 cm⁻¹. *Applied Spectroscopy*, 50(8), 1047–1057. <https://doi.org/10.1366/0003702963905385>
- Boucher, O., Randall, D., Artaxo, P., Bretherton, C., Feingold, G., Forster, P., et al. (2013). In Stocker, T. F., et al. (Eds.), *Climate change 2013: The physical science basis. Contribution of working group I to the fifth assessment report of the intergovernmental panel on climate change*. Cambridge, United Kingdom and New York, NY: Cambridge University Press.
- Cesana, G., Kay, J. E., Chepfer, H., English, J. M., & de Boer, G. (2012). Ubiquitous low-level liquid-containing Arctic clouds: New observations and climate model constraints from CALIPSO-GOCCP. *Geophysical Research Letters*, 39, L20804. <https://doi.org/10.1029/2012GL053385>
- Clough, S., Shephard, M. W., Shephard, M. W., Mlawer, E. J., Delamere, J. S., Iacono, M. J., et al. (2005). Atmospheric radiative transfer modeling: A summary of the AER codes. *Journal of Quantitative Spectroscopy and Radiative Transfer*, 91, 233–244. <https://doi.org/10.1016/j.jqsrt.2004.05.058>
- Conway, T. J., Tans, P. P., Waterman, L. S., Thoning, K. W., Kitzis, D. R., Masarie, K. A., & Zhang, N. (1994). Evidence for interannual variability of the carbon cycle from the National Oceanic and Atmospheric Administration/Climate Monitoring and Diagnostics Laboratory global air sampling network. *Journal of Geophysical Research*, 99(D11), 22831–22855. <https://doi.org/10.1029/94JD01951>
- Cox, C., Rowe, P. M., Neshyba, S. P., & Walden, V. P. (2016). A synthetic data set of high-spectral-resolution infrared spectra for the Arctic Atmosphere. *Earth System Science Data*, 8, 199–211. <https://doi.org/10.5194/essd-8-199-2016>
- Cox, C., Walden, V. P., Rowe, P. M., & Shupe, M. (2015). Humidity trends imply increased sensitivity to clouds in a warming Arctic. *Nature Communications*, 6, 10117. <https://doi.org/10.1038/ncomms10117>
- Downing, H. D., & Williams, D. (1975). Optical constants of water in the infrared. *Journal of Geophysical Research*, 80(12), 1656–1661. <https://doi.org/10.1029/jc080i012p01656>
- Grenfell, T. C., & Warren, S. G. (1999). Representation of a nonspherical ice particle by a collection of independent spheres for scattering and absorption of radiation. *Journal of Geophysical Research*, 104, 31697–31709. <https://doi.org/10.1029/1999jd900496>
- Hansen, J. E., & Travis, L. D. (1974). Light scattering in planetary atmospheres. *Space Science Reviews*, 16, 527–610. <https://doi.org/10.1007/bf00168069>
- Hogan, R. J., Illingworth, A. J., O'Connor, E. J., & Baptista, J. P. (2003). Characteristics of mixed-phase clouds. II. A climatology from ground-based LIDAR. *Quarterly Journal of the Royal Meteorological Society*, 129, 2117–2134. <https://doi.org/10.1256/qj.01.209>
- Hu, Y., Rodier, S., Xu, K., Sun, W., Huang, J., Lin, B., et al. (2010). Occurrence, liquid water content, and fraction of supercooled water clouds from combined CALIOP/IIR/MODIS measurements. *Journal of Geophysical Research*, 115, D00H34. <https://doi.org/10.1029/2009JD012384>
- Koop, T., Luo, B., Tsias, A., & Peter, T. (2000). Water activity as the determinant for homogenous ice nucleation in aqueous solutions. *Nature*, 406, 611–614. <https://doi.org/10.1038/35020537>
- Lawson, R. P., & Gettelman, A. (2014). Impact of Antarctic mixed-phase clouds on climate. *Proceedings of the National Academy of Sciences*, 111, 18156–18161. <https://doi.org/10.1073/pnas.1418197111>
- Lawson, R. P., Stammer, K., Stammer, J. J., Zmarzly, P., Koskuliks, J., Roden, C., et al. (2011). Deployment of a tethered-balloon System for microphysics and radiative measurements in mixed-phase clouds at Ny-Ålesund and South Pole. *Journal of Atmospheric and Oceanic Technology*, 28(5), 656–670. <https://doi.org/10.1175/2010jtecha1439.1>
- Mahesh, A., Campbell, J. R., & Spinhrne, J. D. (2005). Multi-year measurements of cloud base heights at South Pole by LIDAR. *Geophysical Research Letters*, 32, L09812. <https://doi.org/10.1029/2004GL021983>
- Murakami, M., & Matsuo, T. (1990). Development of the hydrometeor vide sonde. *Journal of Atmospheric and Oceanic Technology*, 7, 613–620. [https://doi.org/10.1175/1520-0426\(1990\)007<0613:dothv>2.0.co;2](https://doi.org/10.1175/1520-0426(1990)007<0613:dothv>2.0.co;2)
- Orikasa, N., & Murakami, M. (1997). A new version of hydrometeor vide sonde for cirrus cloud observations. *Journal of the Meteorological Society of Japan*, 75, 1033–1039. https://doi.org/10.2151/jmsj1965.75.6_1033
- Otsu, N. (1979). A thresholding selection method from gray-level histogram. *IEEE Transactions on Systems, Man, and Cybernetics*, 9(1), 62–66. <https://doi.org/10.1109/tsmc.1979.4310076>
- Peters, W., Jacobson, A. R., Sweeney, C., Andrews, A. E., Conway, T. J., Masarie, K., et al. (2007). An atmospheric perspective on North American carbon dioxide exchange: CarbonTracker. *Proceedings of the National Academy of Sciences*, 104(48), 18925–18930. <https://doi.org/10.1073/pnas.0708986104>
- Rodgers, C. D. (2000). *Inverse Methods for Atmospheric Sounding: Theory and Practice* (Vol. 2). Singapore: World Scientific.
- Rosenfeld, D., & Woodley, W. L. (2000). Deep convective clouds with sustained supercooled liquid water down to -37.5°C. *Nature*, 405, 440–442. <https://doi.org/10.1038/35013030>
- Rowe, P., & Walden, V. P. (2009). Improved measurements of the foreign-broadened continuum of water vapor in the 6.3 μm band at -30°C. *Applied Optics*, 48, 1358–1365. <https://doi.org/10.1364/AO.48.001358>
- Rowe, P., Walden, V. P., & Warren, S. G. (2006). Measurements of the foreign-broadened continuum of water vapor in the 6.3-μm band at -30°C. *Applied Optics*, 45(18), 4366–4382. <https://doi.org/10.1364/ao.45.004366>
- Rowe, P. M., Cox, C., Neshyba, S., & Walden, V. P. (2019). Toward autonomous surface-based infrared remote sensing of polar clouds: Retrievals of cloud optical and microphysical properties. *Atmospheric Measurement Techniques*, 12(9), 5071–5086. <https://doi.org/10.5194/amt-12-5071-2019>
- Rowe, P. M., Fergoda, M., & Neshyba, S. (2020). Temperature-dependent optical properties of liquid water from 240 to 298 K. *Journal of Geophysical Research: Atmospheres*, 125(17). <https://doi.org/10.1029/2020JD032624>
- Rowe, P. M., Miloshevich, L. M., Turner, D. D., & Walden, V. P. (2008). Dry bias in Vaisala RS90 radiosonde humidity profiles over Antarctica. *Journal of Atmospheric and Oceanic Technology*, 25(9), 1529–1541. <https://doi.org/10.1175/2008JTECHA1009.1>
- Rowe, P. M., Neshyba, S., Cox, C. J., & Walden, V. P. (2011). A responsivity-based criterion for low noise in FTIR emission spectra: Identification of in-band low-responsivity wavenumbers. *Optics Express*, 19(6), 5451–5463. <https://doi.org/10.1364/OE.19.005451>
- Rowe, P. M., Neshyba, S., & Walden, V. P. (2011). Responsivity-based criterion for accurate calibration of FTIR emission spectra: Theoretical development and bandwidth estimation. *Optics Express*, 19(7), 5930–5941. <https://doi.org/10.1364/OE.19.005930>

- Rowe, P. M., Neshyba, S., & Walden, V. P. (2013). Radiative consequences of low-temperature infrared refractive indices for supercooled water clouds. *Atmospheric Chemistry and Physics*, *13*, 11925–11933. <https://doi.org/10.5194/acp-13-11925-2013>
- Spinirne, J. D. (1993). Micro pulse LIDAR. *IEEE Transactions on Geoscience and Remote Sensing*, *31*, 48–55. <https://doi.org/10.1109/36.210443>
- Stamnes, K., Tsay, S.-C., Wiscombe, W., & Jayaweera, K. (1988). Numerically stable algorithm for discrete-ordinate-method radiative transfer in multiple scattering and emitting layered media. *Applied Optics*, *27*(12), 2502–2509. <https://doi.org/10.1364/ao.27.002502>
- Wagner, R., Benz, S., Möhler, O., Saathoff, H., Schnaiter, M., & Schurath, U. (2005). Mid-infrared Extinction spectra and optical constants of supercooled water droplets. *The Journal of Physical Chemistry A*, *109*(32), 7099–7112. <https://doi.org/10.1021/jp051942z>
- Walden, V. P., Ellison, M. E., Brandt, R. E., Town, M. S., Hudson, S. R., & Jones, R. M. (2005). Properties of super-cooled water clouds over South Pole. In *Proceedings of the 8th conference on polar meteorology and oceanography* (pp. 9–13). San Diego, CA.
- Walden, V. P., Warren, S. G., Spinirne, J. D., Heymsfield, A., Brandt, R. E., Rowe, P., et al. (2001). The South Pole Atmospheric Radiation and Cloud LIDAR Experiment (SPARCLE). In *Proceedings of 6th conference polar meteorology and oceanography* (pp. 297–299). San Diego, CA.
- Warren, S. G., & Brandt, R. E. (2008). Optical constants of ice from the ultraviolet to the microwave: A revised compilation. *Journal of Geophysical Research*, *113*, D14220. <https://doi.org/10.1029/2007JD009744>
- Zasetsky, A. Y., Khalizov, A. F., Earle, M. E., & Sloan, J. J. (2005). Frequency dependent complex refractive indices of supercooled liquid water and ice determined from Aerosol Extinction spectra. *The Journal of Physical Chemistry A*, *109*(12), 2760–2764. <https://doi.org/10.1021/jp044823c>
- Zasetsky, A. Y., Khalizov, A. F., & Sloan, J. J. (2004). Local order and dynamics in supercooled water: A study by IR spectroscopy and molecular dynamic simulations. *Journal of Chemical Physics*, *121*, 6941–6947. <https://doi.org/10.1063/1.1787494>
- Zhang, D., Wang, Z., & Liu, D. (2010). A global view of midlevel liquid- layer topped stratiform cloud distribution and phase partition from CALIPSO and CloudSat measurements. *Journal of Geophysical Research*, *115*, D00H13. <https://doi.org/10.1029/2009JD012143>